SANDIA REPORT
SAND2020-10351
Printed September 2020

Sandia National Laboratories

Tuning the critical Li intercalation concentrations for MoX_2 bilayer phase transitions using classical and machine learning approaches

C.D. Spataru*, M.D. Witman*, R.E. Jones*

Sandia National Laboratories, Livermore, CA 94551

Prepared by
Sandia National Laboratories
Albuquerque, New Mexico 87185
Livermore, California 94550

Issued by Sandia National Laboratories, operated for the United States Department of Energy by National Technology & Engineering Solutions of Sandia, LLC.

Available to DOE and DOE contractors from

U.S. Department of Energy
Office of Scientific and Technical Information
P.O. Box 62
Oak Ridge, TN 37831

Telephone: (865) 576-8401
Facsimile: (865) 576-5728
E-Mail: reports@osti.gov
Online ordering: http://www.osti.gov/scitech

Available to the public from

U.S. Department of Commerce
National Technical Information Service
5301 Shawnee Road
Alexandria, VA 22312

Telephone: (800) 553-6847
Facsimile: (703) 605-6900
E-Mail: orders@ntis.gov
Online order: https://classic.ntis.gov/help/order-methods

ABSTRACT

Transition metal dichalcogenides (TMDs) such as MoX_2 are known to undergo a structural phase transformation as well as a change in the electronic conductivity upon Li intercalation. These properties make them candidates for charge tunable ion-insertion materials that could be used in electro-chemical devices for neuromorphic computing applications. In this work we study the phase stability and electronic structure of Li-intercalated bilayer MoX_2 with X=S, Se or Te. Using first-principles calculations in combination with classical and machine learning modeling approaches we find that the energy needed to stabilize the conductive phase decreases with increasing atomic mass of the chalcogen atom X. A similar decreasing trend is found in the threshold Li concentration where the structural phase transition takes place. While the electronic conductivity increases with increasing ion concentration at low concentrations, we do not observe a conductivity jump at the phase transition point.

CONTENTS

LIST OF FIGURES

1. INTRODUCTION

Autonomous vehicles (AVs) serve our national energy security goals as they offer efficiency opportunities that could enable significant fuel consumption reductions. Unfortunately, with the current technology the electrical power associated with on-board sensing or calculations for driving decisions could reach quite large values of the order of kW. This is a consequence of the fact that Si technology uses about a pJ/operation.

Neuromorphic computing is a novel computing architecture that hold the promise for advanced computing with high energy efficiency, while being well suited for artificial intelligence (AI) tasks. Neuromorphic computing can have a profound impact for securing national economic interest in computation for autonomous vehicles and other sectors that require edge computing. One route for realizing novel devices for neuromorphic computing is to leverage ionic/electronic transport properties in electro-chemical devices. However, a major roadblock in the development of electro-chemical devices is the lack of understanding the fundamental mechanisms that leads to conductivity changes in the ion-insertion material used in neuromorphic devices.

Recently, a novel electro-chemical device called Li-Ion Synaptic Transistor for Low Power Analog Computing (LISTA) has been pioneered at Sandia by Talin et al. [2]. LISTA is 3-terminal redox transistor which allows ion-insertion into a channel by applying a small gate voltage. Through reversible Li intercalation, the channel electronic conductance (synaptic weight) can be gradually changed. Hundreds of conducting states can be modulated in a controllable fashion with switching times ($< \mu$s) comparable to those measured in biological synapses [3, 4] and much lower power ($<$ fJ/operation [2]) than Si-based CMOS transistors.

In order to take the proof-of-concept LISTA device to scalable technology, it is important to understand how it works at a fundamental level. Despite progress on the experimental front, the mechanisms that leads to conductivity changes are not fully understood. In particular it is not clear how the structural and electronic properties of the ion-insertion material evolve as a function of ion concentration. For example, do ions intercalate into the channel in an ideal fashion, *i.e* gradually and with uniform concentration, or rather they form co-existing domains of insulating and metallic phases with sizes that depends on gate voltage? This and other similar questions regarding the equilibrium and nonequilibrium intercalation regimes can be addressed computationally via mesoscopic modeling approaches [1]. However, such models require knowledge of the phase stability diagram as well as the electronic properties of the ion-insertion materials as function of uniform ion concentration. Such knowledge can be obtained via first-principles studies.

From a materials point of view, quasi-two dimensional layered systems are very attractive due to their layered structure. Indeed, they can be very useful in electrochemical devices because the weak van der Waals interaction between layers facilitates ion intercalation. As such, layered systems can find applicability such as *e.g.* electrode materials for batteries with high energy storage. A particular layered material class is represented by transition metal dichalcogenides (TMDs) *i.e.* MoS_2, $MoSe_2$ or $MoTe_2$. These materials undergo a structural phase transformation upon ion intercalation. This transition is accompanied by a change in the electronic conductivity, which makes them candidates for charge tunable ion-insertion materials in electro-chemical

devices for neuromorphic computing applications. Moreover, two-dimensional few-layer TMDs are of interest for small-scale device fabrication which is desirable given that the write energy per operation increases with channel size (resistance) [2]. While there is a large body work on ion intercalation in bulk TMDs [5, 7, 8] or ion adsorption on monolayer TMDs [10], fewer studies have focused so far on few-layer TMDs [9] such as bilayers[11, 12] and more such studies are welcome.

In this work we perform a first-principles based study of the phase stability and electronic structure evolution of Li ion-intercalated bilayer TMDs. We hypothesize that *ab initio* Density Functional Theory (DFT) can be integrated with machine learning to efficiently predict the phase stability and electronic structure evolution of ion-insertion layered materials. We explore this path together with the more established cluster expansion method to obtain thermodynamic properties and ultimately the phase stability diagram.

2. THEORETICAL FRAMEWORK

TMDs may take several polytype forms, such as the semiconducting 2H phase, metallic T phase and semimetallic T' phase. In few-layer TMDs, the metallic T phase is however unstable due to a Peierls distortion that dimerizes the metal atoms leading to the formation of the T' phase. Thus, we consider only two competing phases, namely 2H and T' (see fig. 1-1). A large fraction of our computational effort consists on estimating the free energy of these competing phases, from which a phase diagram will be predicted. Ultimately, this allows us to make predictions regarding the electronic conductivity of Li ion-intercalated bilayer TMDs as function of ion concentration.

2.1. Free energy expressions

To motivate our methodology a brief review of fundamental statistical mechanics is needed. The canonical/Helmholtz (NT) free energy is

$$F(n_{\mathrm{Li}}, T) = k_B T \ln(Z(n_{\mathrm{Li}}, T)) \tag{1}$$

where k_B is Boltzmann's constant, T is temperature, and

$$Z(n_{\mathrm{Li}}, T) = \sum_i \exp\left(-\frac{E_i}{k_B T}\right) \tag{2}$$

is the partition function. For brevity we have suppressed the dependence of the free energy on the system stress as we focus on fully relaxed systems *i.e.* at zero stress. In Eq. (2) the sum is over all possible configurations with n_{Li} lithium atoms, and the energy E_i is energy of configuration χ_i relative to a chosen reference state. A minimum in $F(n_{\mathrm{Li}})$ indicates the most likely concentration of Li. The difference $\Delta F = F_{2\mathrm{H}} - F_{\mathrm{T'}}$ between phases indicates which phase is more stable (and eliminates the dependence on a reference state).

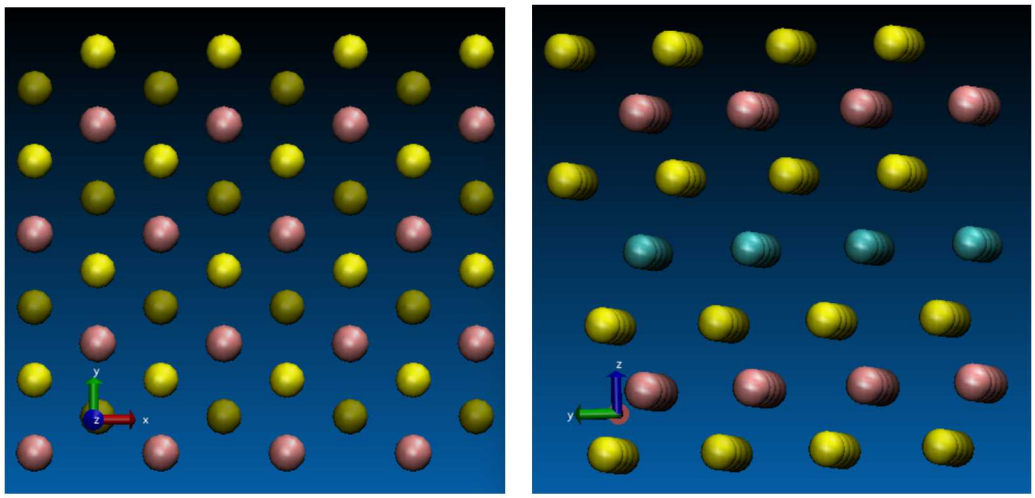

(a) 2H

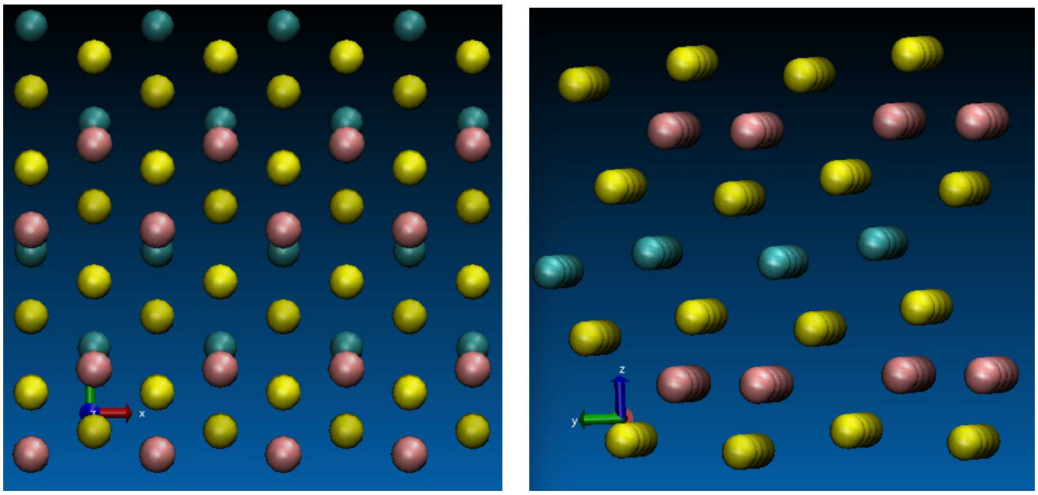

(b) T'

Figure 1-1 Atomic structure of bilayer MoX_2 layered material (a) 2H phase and (b) T' phase. Left panels: top view. Right panels: side view. Color code for balls: Red = Mo; Yellow=X; Blue: Li.

The grand canonical free energy (μT) takes a similar form

$$\Phi(\mu, T) = k_B T \ln(\Omega(\mu, T)) \tag{3}$$

where the partition function is

$$\Omega(\mu, T) = \sum_i \exp\left(\frac{\mu n_i}{k_B T}\right) Z(n_i, T) \tag{4}$$

In this case the sum is over all possible configurations (from $n_{\mathrm{Li}} = 0$ up to $n_{\mathrm{Li}} = n_{\max}$ at saturation of all low energy sites). With Φ the average number of Li can be computed:

$$\langle n \rangle_{\mu\mathrm{T}} = -\frac{\partial \Phi}{\partial \mu} = \sum_{i=0}^{n_{\max}} n_i \frac{\exp\left(\frac{\mu n_i}{k_B T}\right) Z(n_i, T)}{\Omega(\mu, T)} \tag{5}$$

The grand canonical potential informs us about how many Li reside on/in the bilayer if there is an environmental reservoir of lithium (as in a electrochemical device) specified by the chemical potential μ.

In these free energy expressions the contribution to the entropy comes entirely from the configurational degrees of freedom. We omit dependence on vibrational modes, electronic modes, etc.. While the vibrational entropy can be significant, its contribution to the free energy difference between phases is expected to be minor; the variation of the vibrational entropy across phases of the same chemical species is typically small so that it does not affect significantly the relative phase stability [13, 14]. Similarly, while the configurational entropy may converge slowly with system size, its variation between chemically similar phases is expected to converge fast enough to make it tractable to compute with feasible system/supercell sizes.

2.2. Method for obtaining total energies

To calculate the relative free energies and thus the phase diagram we need a set of energies $\{E_i\}$ that sample the configurational space of each phase. We obtain these from first principles via DFT calculations and hence are limited to small systems with a fixed number of bilayer lattice atoms and varying number of intercalated lithium atoms. The configurational space of these small systems can be sampled exhaustively using a surrogate model. We explored a number of surrogate models: (a) cluster expansion, (b) an image based transfer learning neural network, and (c) a graph convolution neural network.

2.2.1. *Ab initio* calculations

We calculate total energies as well as the electronic density of states (DOS) of Li ion-intercalated bilayer TMD structures within the framework of *ab initio* DFT using the VASP code [15, 16]. We use projector augmented wave (PAW) pseudo-potentials [17] and treat the exchange and

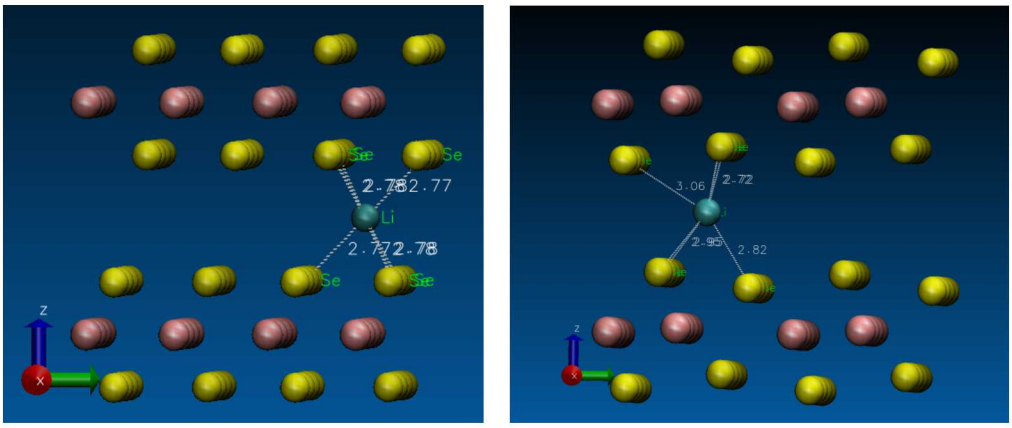

(a) 2H **(b)** T'

Figure 2-1 Side view of the atomic structure of bilayer $MoSe_2$ intercalated with a single Li ion. a) 2H phase. b) T' phase. Color code for balls: Red = Mo; Yellow=Se; Blue: Li.

correlation terms within the generalized gradient approximation with the PBE parameterization [18]. The energy cutoff was set to 400 eV.

We consider bilayer structures where the two monolayers are rotated by 180° with respect to each other. The translational alignment between the two MoX_2 monolayers is such that the Mo atoms are vertically aligned, since we find the energy for this configuration to be the lower than for other alignments.

We construct relatively small systems using supercells obtained by replicating in the x-y plane the rectangular unit cell of bilayer MoX_2 with X=S, Se or Te. We use 4×2 lateral replicas with lateral area of about 1.4×1.2 nm^2 and vacuum separation along the z-direction of more than 15 Å. There are 32 Mo atoms and 64 X atoms in our supercells in the absence of ion intercalation, and $n_{\max} = 16$ lithium atoms at saturation of the low energy sites.

There is a large configurational space associated with Li ion intercalation in between the MoX_2 monolayers of the bilayer. To explore the configurational space it is sufficient to sample only stable configurations as they carry most of the weight given that they correspond to local energy minima hence are representative of a large number of configurations. For each phase we identify low energy ion-intercalation sites and select the most stable one, as we find that it has an energy several hundred meV lower than the other, metastable configurations. In the case of the 2H phase we find that the Li ion is most stable when positioned half-way in between two vertically aligned Mo atoms from different monolayers (see fig. 2-1a)) [12]. This results in octahedral coordination to the X atoms (with bond length of about 2.8 Å). In the T' case the most stable Li site is not vertically aligned with Mo while coordination with the closest six X neighbors is distorted from the ideal octahedral case with four different bond lengths ranging from 2.72 Å to 3.06 Å (see fig. 2-1b). We have also checked in the MoS_2 case (for both phases) that Li ion adsorption yields an energy significantly larger (by more than 100 meV) than Li ion intercalation, hence the focus of this work is on ion intercalation.

The Li ion-intercalation sites form a 16-site layer sublattice, *i.e.* there is one possible Li intercalation site for each Mo_2X_4 bilayer formula unit. The Li-concentration x in the stoichiometric formula Li_xMoX_2 ranges from $x = 0$ (no intercalation, $n_{Li} = 0$) to $x = 0.5$ at full ($n_{\mathrm{Li}} = 16$) Li sublattice occupancy. The number of possible configurations for fixed n_{Li} is $n_{\mathrm{max}}!/(n_{\mathrm{Li}}!(n_{\mathrm{max}} - n_{\mathrm{Li}})!)$. Summing over n_{Li} from 0 to 16 brings the total number of possible configurations to 65536 per system/phase. We do not consider mixtures of phases (domains) in the lateral (x-y) directions nor the possibility that two monolayers could belong to a different phase.

For each of the three MoX_2 systems and for both 2H and T' phases we random sample the configurational space with the number of intercalated Li ions n_{Li} spanning the entire range from 0 to $n_{max} = 16$. More exactly we study from first principles via DFT about 300 such configurations approximately uniformly sampled across concentrations for each system/phase. Each configuration is geometrically optimized by minimizing the stress tensor and relaxing the atomic forces to better than 0.005 eV/ Å. During optimization the Brillouin zone is sampled with a $4\times4\times1$ k-point grid. Convergence in the electronic density of states of the relaxed structures is achieved with a $10\times10\times1$ k-point grid size.

2.2.2. Cluster expansion method

Predicting the total energy of all possible distinct initial configurations is computationally too intensive within *ab initio* DFT even for the relatively small 4×2 supercell. To this end we employ several models that can sample exhaustively the entire configurational space. The first we consider is the Cluster expansion (CE) method [19, 20, 21], a classical technique based on a linear coefficient model with a nearest neighbor expansion

$$E = E_{\mathrm{CE}} = c_0 + \sum_a c_a f_a \tag{6}$$

where the features f_a are formed from a polynomial expansion of binned nearest neighbors. Here n_b is the total number of neighbors in the b-th bin. The bins we consider are annular rings with width small enough such that they contain one type of neighbors. In a n-th order expansion f_a would be complete in powers of n_a up to n_{CE}. The coefficients c_a are found via regression. In the standard form, the polynomial order is set to $n_{CE} = 1$. We have explored higher order polynomials as well, *i.e.* $n_{CE} \leq 3$ [22].

2.2.3. Machine learning methods

We have used several deep learning techniques such as crystal graph convolutional neural network (CGCNN) [23] and transfer learning [24] of a pretrained image classification network.

The CGCNN formalism is based on a universal and interpretable representation of crystalline materials. A crystallographic structure is interpreted as a graph whose nodes, corresponding to atoms, are connected by edges, corresponding to bonds, with surrounding atoms. Each node and edge is initialized with a vector of attributes (i.e., these could be elemental properties of a given

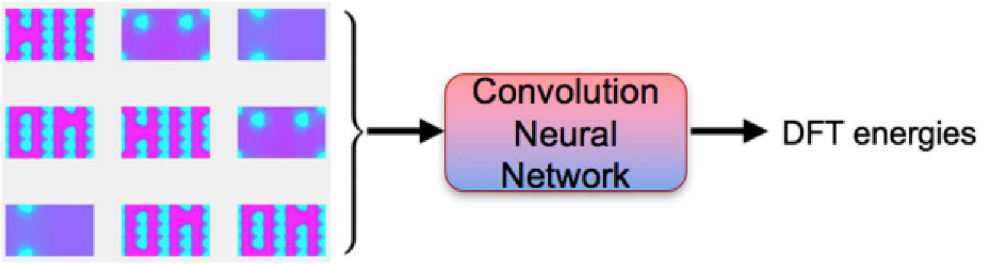

Figure 2-2 Illustration of how electrostatic potentials due to ions + unrelaxed electronic orbitals can be used as input to re-trained deep neural networks to predict total energies.

atom and a Gaussian smeared distance of a bond). The CGCNN architecture then applies a nonlinear graph convolution functions that iteratively update the atoms' feature vectors with the surrounding atoms and bonds. Critically, a pooling layer then produces an overall feature vector for the entire crystal that satisfies invariance with respect to atom indexing (permutational invariance) and number of atoms in the unit cell (size invariance). Training is performed to minimize the difference between the CGCNN predicted property and, for example, DFT computed formation energy of that crystal structure. Details can be found in [23], so we simply write that the CGCNN function f, given parameterized weights $\mathbf{W}$ and crystal structure χ, provides a model for the DFT predicted energy formation energy

$$E_{\mathrm{CGCNN}} = f(\chi; \mathbf{W}). \tag{7}$$

We have also applied a transfer learning technique to an existing convolutional neural network (CNN) originally trained on image recognition. To this end we have used *googlenet*, a 22-layer deep CNN that has already learned to extract features from images. We replace the replace outer, classification layer with a new regression layer and use transfer learning to re-train the network on predicting energies based on images of the electrostatic potential field (see fig. 2-2).

Within both approaches the training set consists of hundreds of inputs and outputs. CGCNN uses as input the atomic coordinates while within our transfer learning approach we use images of the non-self-consistent electrostatic potential projected on a plane that passed through the Li-ion layer. In both cases the output are the self-consistent DFT total energies.

3. SURROGATE MODEL COMPARISON

3.1. Monolayer MoS_2 2H phase

We first compared the surrogate models using a less computationally intensive (but artificial) system, namely an unrelaxed MoS_2 monolayer (ML) in the 2H form. We have generated 2550 configurations with Li ion randomly adsorbed on one face of the ML, with the possible adsorption

sites forming a 16-site Li sublattice. The DFT calculations are carried non-self-consistently, hence they are fast computationally but the output energies do not have physical significance.

Prior to the training process we transform total energies E into formation energies $\tilde{E}$ according to a linear transformation:

$$\tilde{E}_i = E_i - n_i[E(n_{Li} = n_{\max}) - E(n_{Li} = 0)]/n_{\max} - E(n_{Li} = 0) \tag{8}$$

This transformation reduces the energy range of the outputs by more than an order of magnitude, from about 50 eV to about 3 eV (see fig. 3-1, which facilitates faster convergence during the training process within the machine learning approaches.

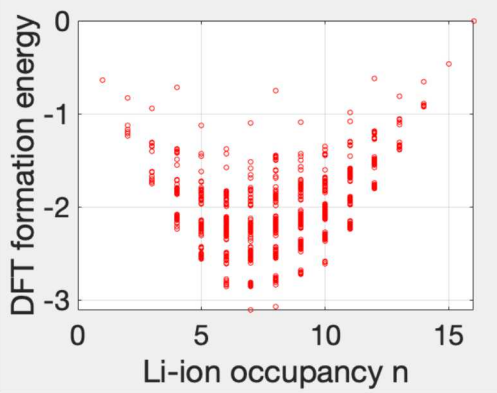

Figure 3-1 DFT formation energies of ML MoS_2 as function of the number of adsorbed Li ions per supercell.

Fig. 3-2 shows the performance of the CE method for predicting the energies of ML MoS_2. In the standard version ($n_{CE} = 1$), one achieves relatively good prediction accuracy with a mean average error (MAE) of 36 meV. However, we find a significant improvement by increasing n_{CE} to 2.

Fig. 3-3 shows similar results obtained via the two machine learning techniques mentioned earlier. Panels a) and b) show the prediction error and predicted energies obtained within CGCNN. In this case we find that the MAE is 20 meV. Panel c) shows the prediction error obtained within the transfer learning technique for one particular retraining run which yields a MAE of 29 meV. We find that fine-tuning within the transfer learning process yields MAE lower than 20 meV, *.i.e.* on par with CGCNN. Since CGCNN is a more established technique for predicting energies of physical systems than the transfer learning approach, we decided to use only CGCNN for the rest of our machine learning simulations.

3.2. Bilayer MoS_2 T' phase: average Li concentration as function of Li chemical potential.

We have also compared CE and CGCNN using a realistic system, namely Li ion intercalated bilayer MoS_2 (T' phase). We generated 2500 configurations with Li ion intercalated in between the monolayers and positioned randomly on a 16-site Li sublattice. The output energies were

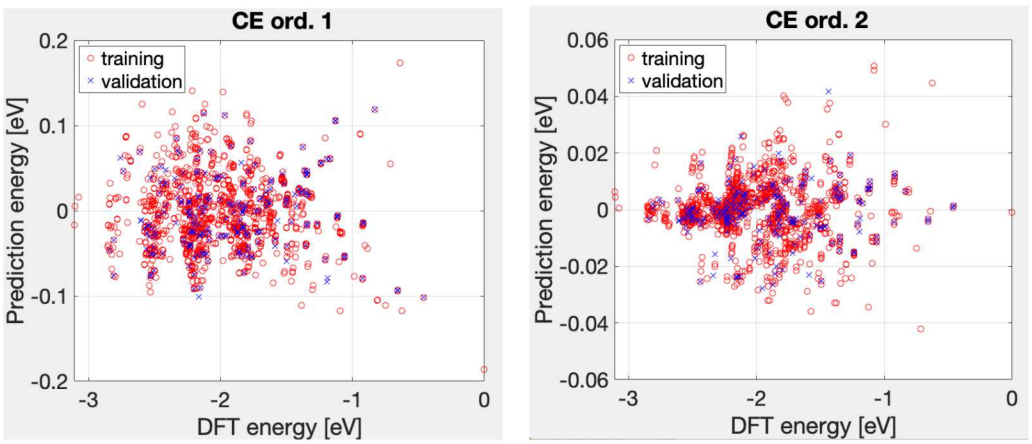

(a) Prediction error

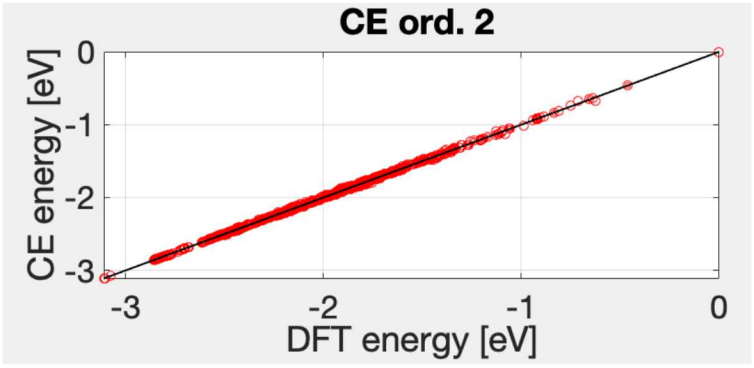

(b) Predicted energy

Figure 3-2 Illustration of the CE method applied to ML MoS_2. Prediction errors for a) $n_{CE} = 1$ and b) $n_{CE} = 2$. c) Comparison between the DFT formation energies and those predicted within CE with $n_{CE} = 2$.

obtained self-consistently within DFT, and relaxation of forces and stress was performed for each configuration. CE ad CGCNN trained on a 80% subset of the data with the rest of configurations being used for validation. The predicted energies were used to construct the grand canonical potential as well as the statistical average of the number of Li ions $\langle N \rangle$ as function of Li chemical potential. We find that differences between the two surrogate methods manifest themselves most evidently in $\langle N \rangle >$, thus we focus on the quantity next.

Fig. 3-4 shows $\langle N \rangle >$ vs. the Li chemical potential μ for a relatively large range of μ, calculated based on energy predictions made via either CE or CGCNN. We estimated the chemical potential in a Li-rich environment $\mu^{Li-rich}$ from the DFT binding energy of elemental Li metal and find that $\mu^{Li-rich} \approx -2$ eV. Both CE and CGCNN predict that in a Li-rich environment intercalation is complete, *i.e.* the Li ion concentration saturates to $x = 0.5$ Li ions / formula unit. The two models agree overall up to $|\mu| < 4.1$ eV and even beyond this threshold one compares CGCNN with standard CE ($n_{CE} = 1$). The agreement between standard CE and CGCNN correlates with the fact that they also yield a similar MAE$\approx$ 50 meV. Based on the more accurate energy prediction (MAE$\approx$ 26 meV) within CE with $n_{CE} = 3$, the region near low Li occupancy ($\langle N \rangle \approx 1$) or high chemical potential ($|\mu| < 4.25$) is probably not fully converged within CGCNN. Throughout the

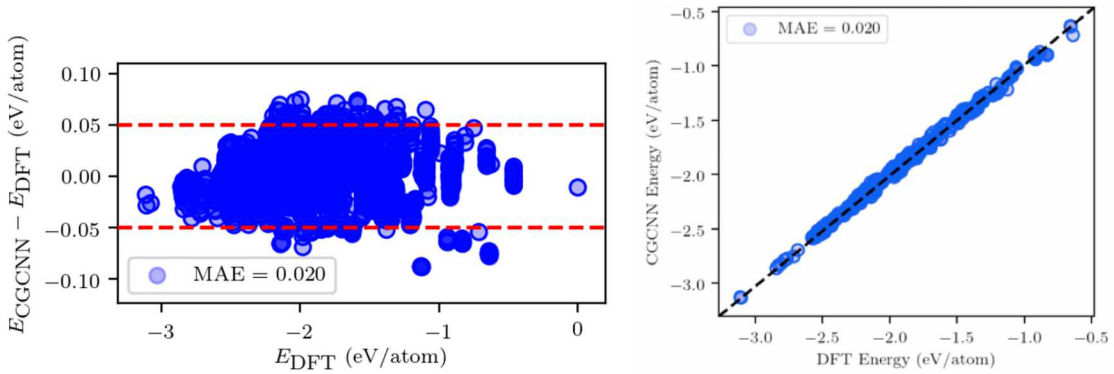

(a) CGCNN

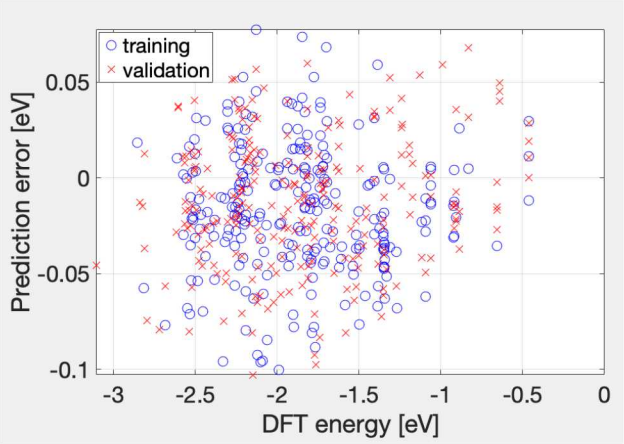

(b) Transfer learning

Figure 3-3 Illustration of two machine learning methods applied to ML MoS_2. a) and b) respectively: CGCNN prediction errors and predicted energies. c) Prediction error within the transfer learning approach.

rest of the paper we will only show results obtained within CE.

4. RESULTS: PHASE STABILITY AND ELECTRONIC STRUCTURE EVOLUTION

4.1. Free energies and phase diagrams

Depending on the experimental conditions, the phase stability of Li ion intercalated bilayer TMDs should be studied either within the canonical (NT) or the grand-canonical (μT) ensemble.

Figure 4-1 shows the Helmholtz (NT) free energy (left panels) and grand-canonical free energies (μT) for three Li ion intercalated bilayer systems: MoS_2, $MoSe_2$, and $MoTe_2$, with temperature T set to room temperature T=300 K.

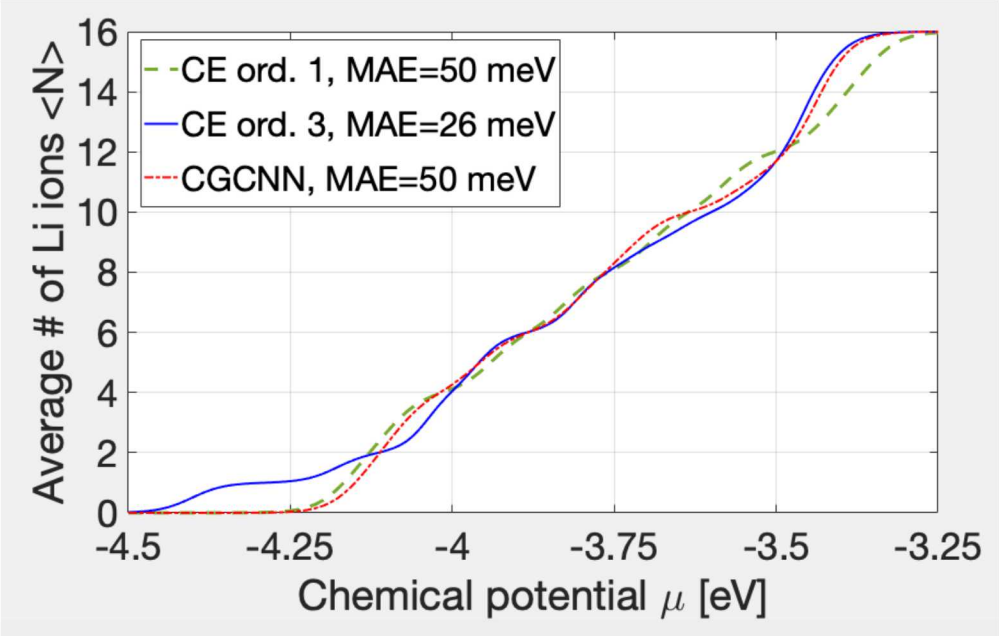

Figure 3-4 Grand-canonical statistical average of the number of Li ions as function of Li chemical potential for MoS_2 T' phase. $T = 300$ **K.**

It appears that the T' phase is preferred at high ion concentrations/low chemical potentials, as its free energy becomes lower that the one of the 2H phase. Interestingly, as the chalcogen atom X gets heavier, the energy needed to stabilize the T' phase smaller and the threshold ion concentration/ chemical potentials where the 2H-T' transition takes place gets smaller/higher.

This trend can be clearly seen in fig. 4-2 which shows the phase diagram at T=300 K for the three bilayer systems.

The upper plot shows that the stabilization energy of the T' phase decreases from ≈ 0.55 eV / formula unit for MoS_2, to ≈ 0.35 eV for $MoSe_2$ and finally decreases to only ≈ 50 meV in the case of $MoTe_2$. A similar trend has been discovered in the case of Li ion adsorption onto ML MoX_2 [25]. Besides the stabilization energy, the threshold Li concentration where the 2H$\leftrightarrow$T' transition happens decreases as well, from $x \approx 0.4$ ions/formula unit for MoS_2, to $x \approx 0.3$ ions/formula unit for $MoSe_2$ and finally to $x \approx 0.05$ ions/formula unit in the case of $MoTe_2$. Similarly, the lower plot in fig. 4-2 shows that the Li chemical potential threshold decreases as well as the chalcogen atom X goes down on group 16 of the periodic table. As mentioned previously, in a rich Li environment, the bilayers are likely taking the T' form and are fully intercalated.

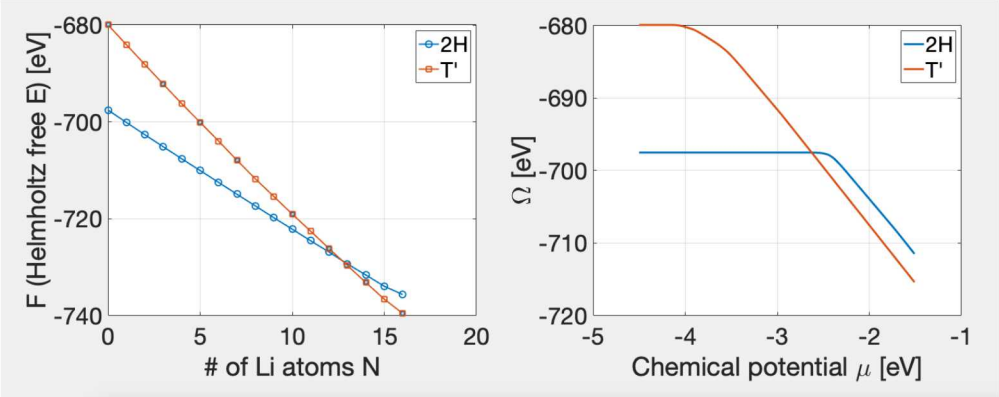

(a) MoS_2

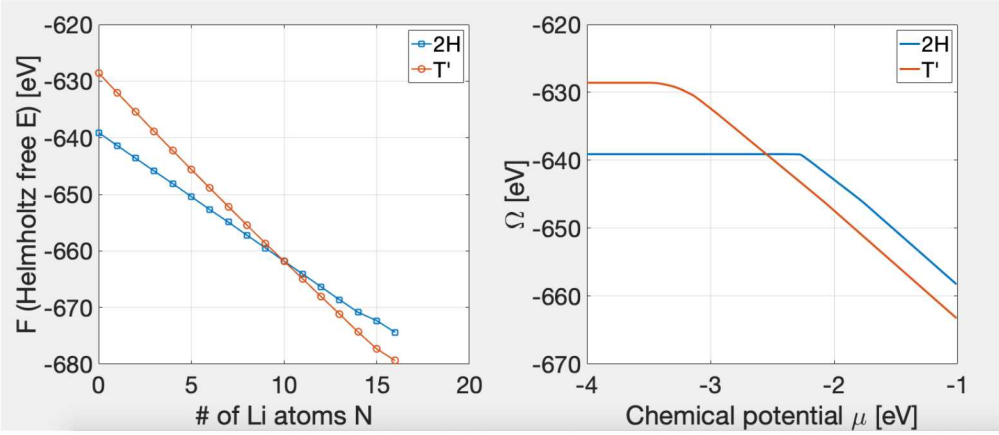

(b) $MoSe_2$

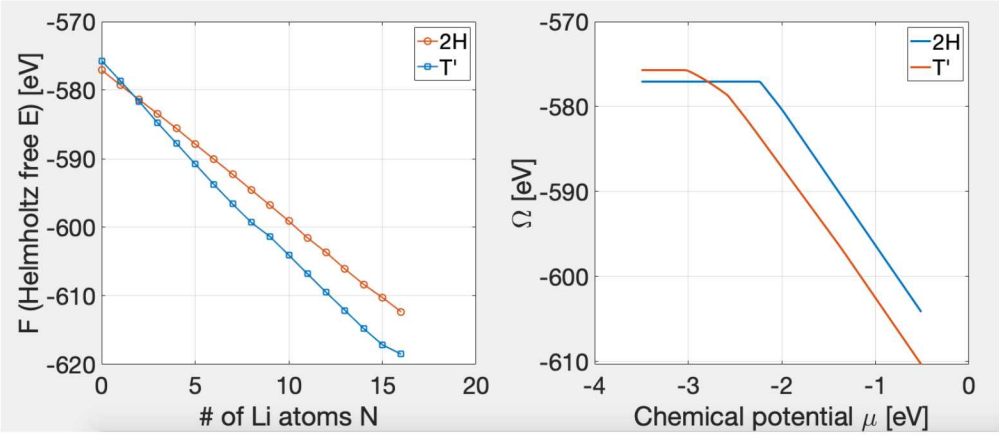

(c) $MoTe_2$

Figure 4-1 Canonical (left panels) and grand canonical (right panels) free energies for: a) MoS_2, b) $MoSe_2$, and c) $MoTe_2$ Li ion intercalated bilayers. $T = 300$ K.

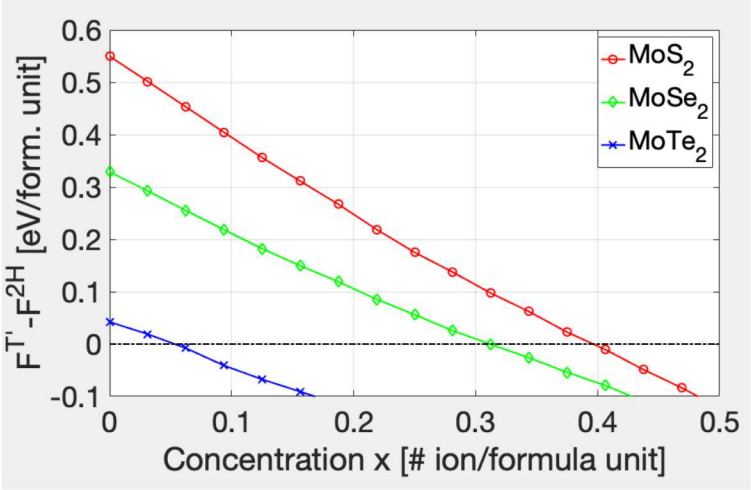

(a) Canonical ensemble

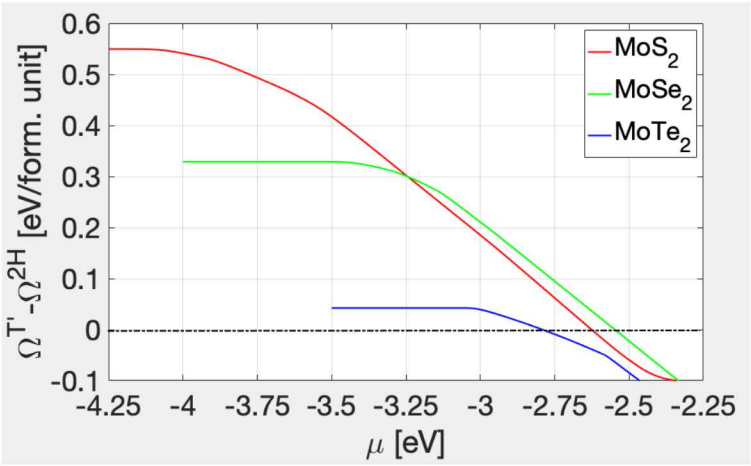

(b) Grand canonical ensemble

Figure 4-2 Free energy differences between competing phases for three Li ion intercalated bilayer MoX_2 TMDs (X=S,Se and Te) obtained within the: a) Canonical, b) Grand canonical picture. $T = 300$ K.

4.2. Density of electronic states

4.2.1. Trends in the DOS with increasing ion concentration

To make predictions regarding the electronic conductivity of Li ion-intercalated bilayer TMDs as function of ion concentration we consider the electronic density of states (DOS) near the Fermi level (E_F) for each system/phase. Indeed, within band theory DOS(E_F) is directly proportional to the electronic conductivity.

Fig. 4-3 shows the DOS as function of electron energy for $MoSe_2$. Left panels refers to the case of no Li ion intercalation. We notice that the 2H is semiconducting while the T' phase is semimetallic. The right panel shows a similar quantity but for the case where one Li ion/supercell

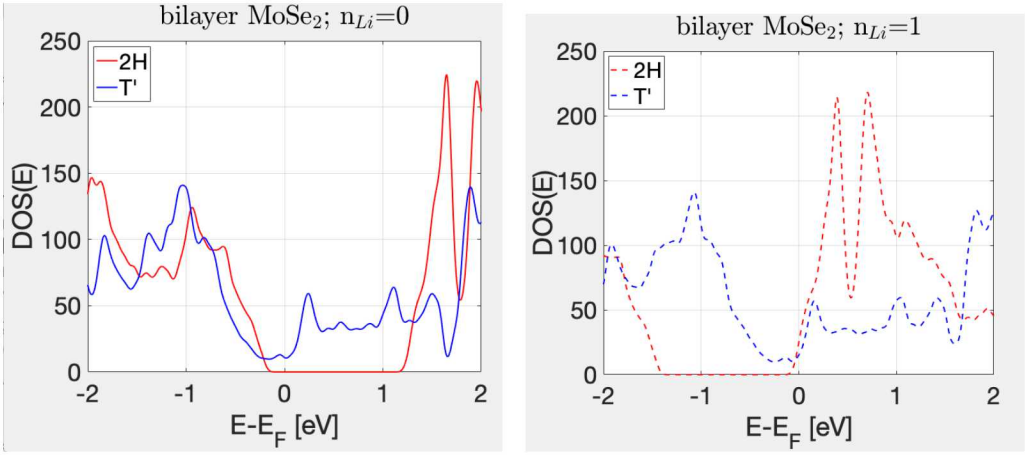

Figure 4-3 Electronic density of states as function of the electron energy measured from the Fermi level E_F for bilayer $MoSe_2$ with: a) no Li ion intercalation, b) one intercalated Li ion per supercell.

is intercalated in the bilayer. We note that for this doping level the DOS of both phases do not renormalize appreciably. Instead, they can be obtained from the no-intercalation case by a simple shift-up of the Fermi level. Due to the semiconducting band gap in the 2H case, the shift to the left of the DOS is correspondingly large > 1 eV. Similarly the DOS shift in the semi-metallic T' case is very small. Because of this, the change in the DOS(E_F) with low Li ion concentration is expected to be small in the latter case while it can be large in the former one.

With larger ion concentration it is possible that the DOS renormalizes, *i.e.* cannot be obtained from the no-intercalation case by a simple shift. This can be seen in fig. 4-4 which shows the DOS of bilayer MoS_2 (T' phase) for several intercalation levels. As previously noticed, at low ion concentration the DOS can be obtained from the no-intercalation case by a simple, small shift (compare blue and red lines). However, in the case of half-occupancy of the Li sublattice (x=0.25 ions/supercell), the DOS shows very low DOS(E_F), clearly a renormalization feature that is not evident for x=0.

4.2.2. Evolution of DOS(E_F) with ion concentration

The evolution of DOS(E_F) with ion concentration is obtained within the canonical ensemble by statistically averaging the DFT calculated DOS(E_F) for each of the ≈ 300 configurations per bilayer system/phase. We do not use a surrogate model to estimate DOS(E_F) in the entire configurational space, as we find that the CE method does not perform well when the training output consists of DOS values (as opposed to total energies).

Fig. 4-5 illustrates in the case of the bilayer MoS_2, our procedure for obtaining from the raw DFT data the statistically averaged DOS(E_F) as function of ion concentration. We note the peculiar feature of very small DOS(E_F) for the T' phase at half Li sublattice occupancy.

Fig. 4-6 summarizes our results for the evolution of DOS(E_F) for each of the bilayer system/phase. We note that for all three systems, DOS(E_F) increases faster for the 2H phase than

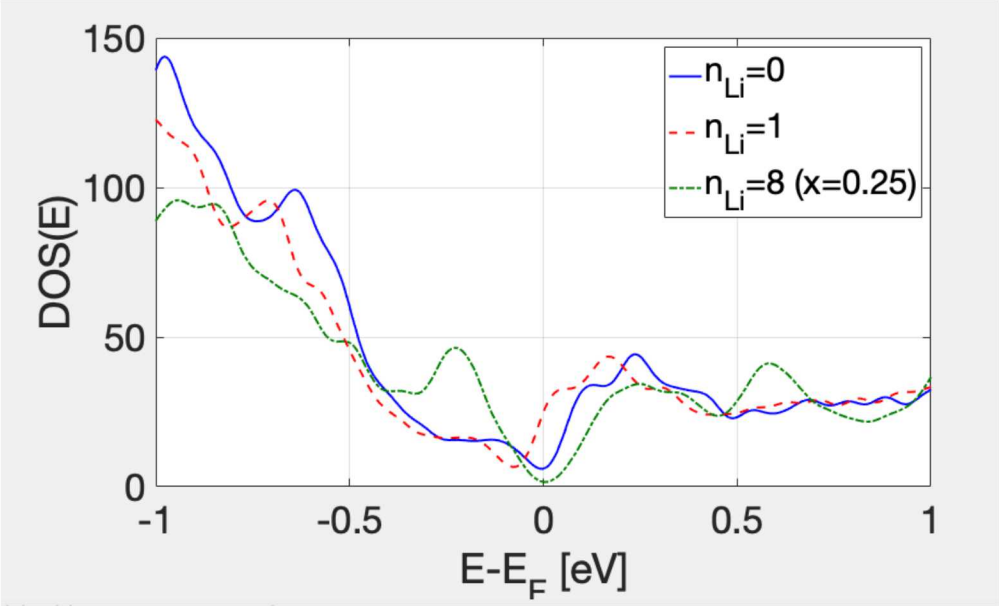

Figure 4-4 Density of states of Li ion intercalated bilayer MoS_2 T' phase for several ion concentrations.

for the T', such that at relatively low ion concentration the 2H phase is the most conductive despite the fact that in the no-intercalation case it is semiconducting. In general, as the concentration increases the 2H remains the most conductive, with the peculiar situation in the MoS_2 case where the T' phase seems to show very low conductivity near half Li sublattice occupancy ($x \approx 0.25$). Importantly, as opposed to the expectation that a change in phase structure from 2H to T' correlates with a jump in electronic conductivity, we do not find this to hold for any of the three bilayer TMDs. In fact our results suggest that as the system transitions between the two phases, the conductivity suffers a decrease instead of a jump.

5. CONCLUSION

We have studied the phase stability and electronic structure evolution of Li-intercalated bilayer MoX_2 with X=S, Se or Te. Using first-principles calculations in combination with classical and machine learning approaches we find that the energy needed to stabilize the T' phase over the 2H one decreases with increasing atomic mass of the chalcogen atom X. A similar decreasing trend is found in the threshold Li concentration where the structural phase transition takes place. While the electronic conductivity increases with increasing ion concentration at low concentrations, we do not observe a conductivity jump at the 2H-T' phase transition point.

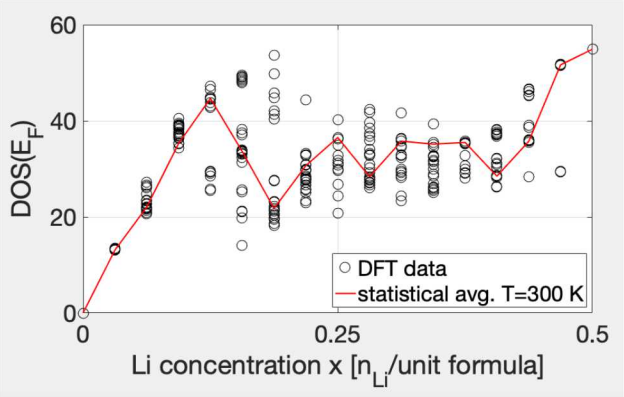

(a) MoS_2, 2H phase

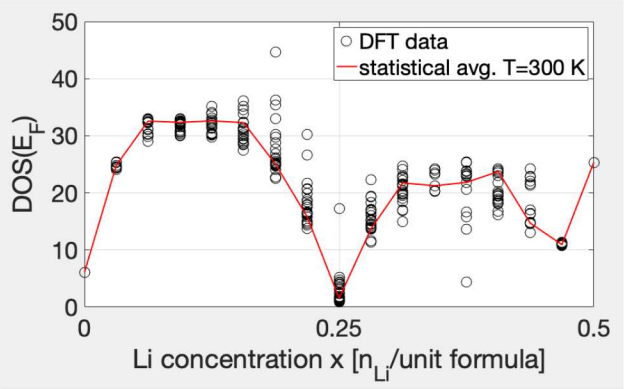

(b) MoS_2, T' phase

Figure 4-5 Density of states at the Fermi level of Li ion intercalated bilayer MoS_2 for the two competing phases: a) 2H, b) T'. $T = 300$ **K.**

ACKNOWLEDGMENTS

This work was supported by the LDRD program at Sandia National Laboratories, and its support is gratefully acknowledged. Sandia National Laboratories is a multimission laboratory managed and operated by National Technology and Engineering Solutions of Sandia, LLC., a wholly owned subsidiary of Honeywell International, Inc., for the U.S. Department of Energy's National Nuclear Security Administration under contract DE-NA0003525. The views expressed in the article do not necessarily represent the views of the U.S. Department of Energy or the United States Government.

REFERENCES

[1] M. Nadkarni, T. Zhou, D. Fraggedakis, T. Gao, and M. Z. Bazant, Adv. Funct. Mater. **29**, 1902821 (2019).

[2] Fuller et al., Adv. Mater. **29**, 1604310 (2017).

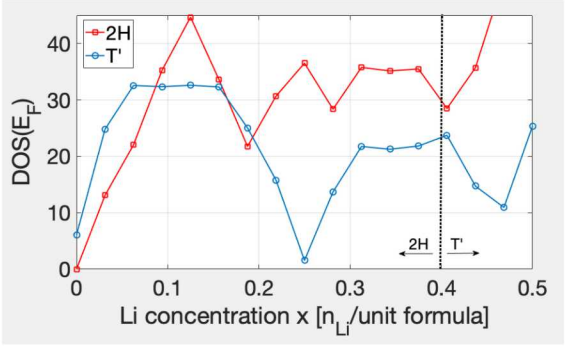

(a) MoS_2

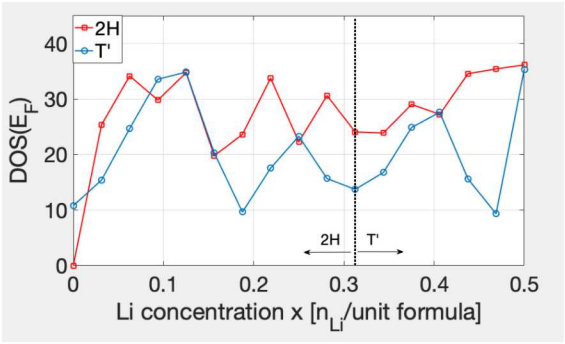

(b) $MoSe_2$

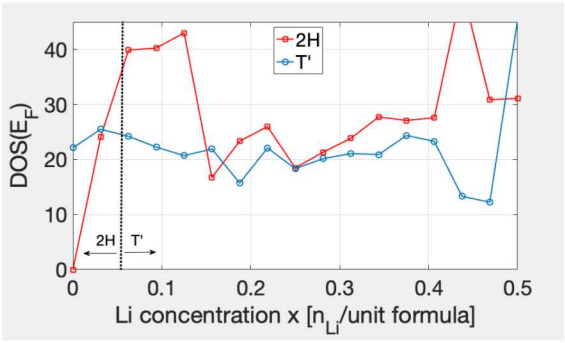

(c) $MoTe_2$

Figure 4-6 Density of states at the Fermi level obtained by statistical average within the canonical ensemble for the two competing phases of Li ion intercalated bilayers: a) MoS_2, b) $MoSe_2$, and c) $MoTe_2$. $T = 300$ **K. The dotted-dashed vertical lines indicates the ion concentrations where the systems transition form 2H to T' phase.**

[3] Fuller et al., Science **364**, 570, (2019).

[4] C.-S. Yang et al.,Adv. Funct. Mater. **28**, 1804170, (2018).

[5] A. N. Enyashin, G. Seifert, Comp. Theor. Chem. **999**, 13 (2012).

[6] D. Nasr Esfahani, O. Leenaerts, H. Sahin, B. Partoens, and F. M. Peeters, J. Phys. Chem. C, **119**, 10602 (2015).

[7] E. Benavente, M.A. Santa Ana, F. Mendizabal, G. Gonzalez, Coord. Chem. Reviews **224**, 87 (2002).

[8] W. Zhao et al., Chem. Eur. J. **24**, 15942 (2018).

[9] J. Zhang et al., Nat. Comm. **9**, 5289 (2018).

[10] X. Sun, Z. Wang, Z. Li and Y. Q. Fu, Scientific Rep. **6**, 26666 (2016).

[11] M. Pandey, P. Bothra, and S. K. Pati J. Phys. Chem. C /bf 120, 3776 (2016).

[12] Z. Lu, S. Carr, D. T. Larson, and E. Kaxiras Phys. Rev. B **102**, 125424 (2020).

[13] A. Urban, D.-H. Seo and G. Ceder, npj Computational Materials **2**, 16002 (2016).

[14] A. Van der Ven, M. K. Aydinol, G. Ceder, G. Kresse and J. Hafner, Phys. Rev. B **58**, 2975 (1998).

[15] We relied on VASP (https://www.vasp.at) to perform *ab initio* calculations.

[16] G. Kresse, and J. Furthmüller, Phys. Rev. B **54**, 11169 (1996).

[17] P. E. Blöchl, Phys. Rev. B **50**, 17953 (1994).

[18] J. P. Perdew, K. Burke, and M. Ernzerhof, Phys. Rev. Lett. **77**, 3865 (1996).

[19] J. M. Sanchez, F. Ducastelle, D. Gratias, Phys A **128**, 334–350 (1984).

[20] D.D. Fontaine, Solid State Phys. **47**, 33–176 (1994).

[21] W. Li, J. N Reimers, J. R. Dahn, Phys. Rev. B **49**, 826 (1994).

[22] Int. J. Scientif. Eng. Research, **4**, 962, (2013).

[23] T. Xie and J. C. Grossman, Phys. Rev. Lett. **120**, 145301 (2018).

[24] We relied on MATLAB (ver. R2018b) to perform the transfer learning technique (https://www.mathworks.com/help/deeplearning/gs/get-started-with-transfer-learning.html).

[25] W. Li and J. Li, Nat. Comm. 7 10843 (2016).

Sandia National Laboratories is a multimission laboratory managed and operated by National Technology & Engineering Solutions of Sandia LLC, a wholly owned subsidiary of Honeywell International Inc., for the U.S. Department of Energy's National Nuclear Security Administration under contract DE-NA0003525.